Electronic Supplementary Information

Overcoming Rate-determining Sodium Kinetics of $Na_3V_2O_2(PO_4)_2F$ Cathode for Ultrafast Sodium Storage by Heterostructured Dual-Carbon Decoration

Xiangyi Li,‡[ab] Shuli Jiang,‡[ab] Shiyu Li,[ab] Junyi Yao,[ab] Yue Zhao,[ab] Tariq Bashir,[ab] Shaowen Zhou,[ab] Shiqi Yang,[ab] Wanying Li,[ab] Wenhao Zhu,[ab] Tingting Liu,[c] Jianqing Zhao,*[ab] Lijun Gao*[ab]

[a] College of Energy, Soochow Institute for Energy and Materials InnovationS, Soochow University, Suzhou 215006, China.

[b] Key Laboratory of Advanced Carbon Materials and Wearable Energy Technologies of Jiangsu Province, Soochow University, Suzhou 215006, China.

[c] Suzhou University of Science and Technology & Jiangsu Key Laboratory of Environmental Science and Engineering, Suzhou 215001, China.

*Corresponding authors:

Prof. Lijun Gao, E-mail: gaolijun@suda.edu.cn

Prof. Jianqing Zhao, E-mail: jqzhao@suda.edu.cn

‡ These two authors equally contributed to this work.

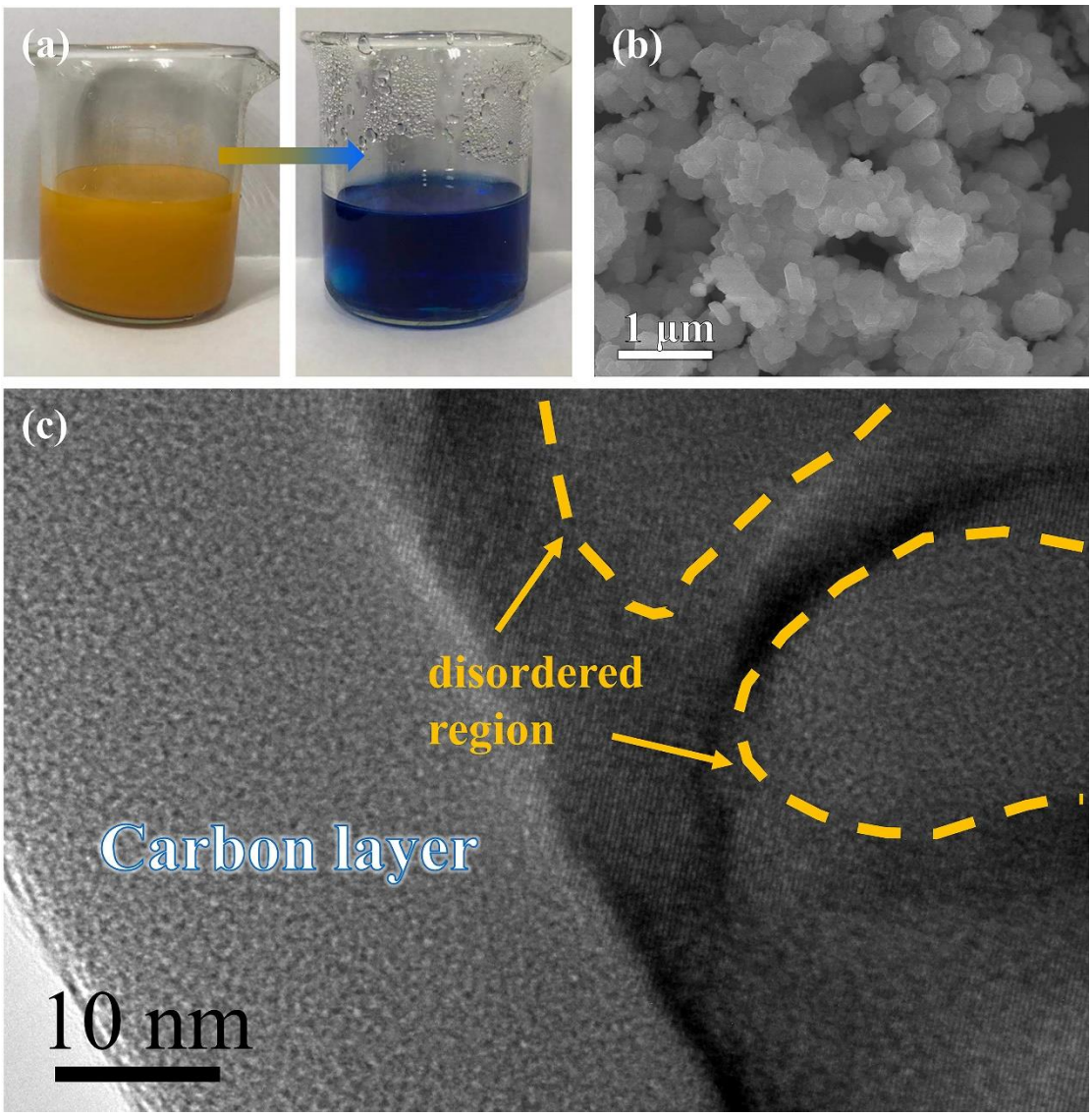

Figure S1. (a) Photographs showing the color change during the reduction of V_2O_5. (b) FESEM image and (c) HRTEM image of NVOPF@C material.

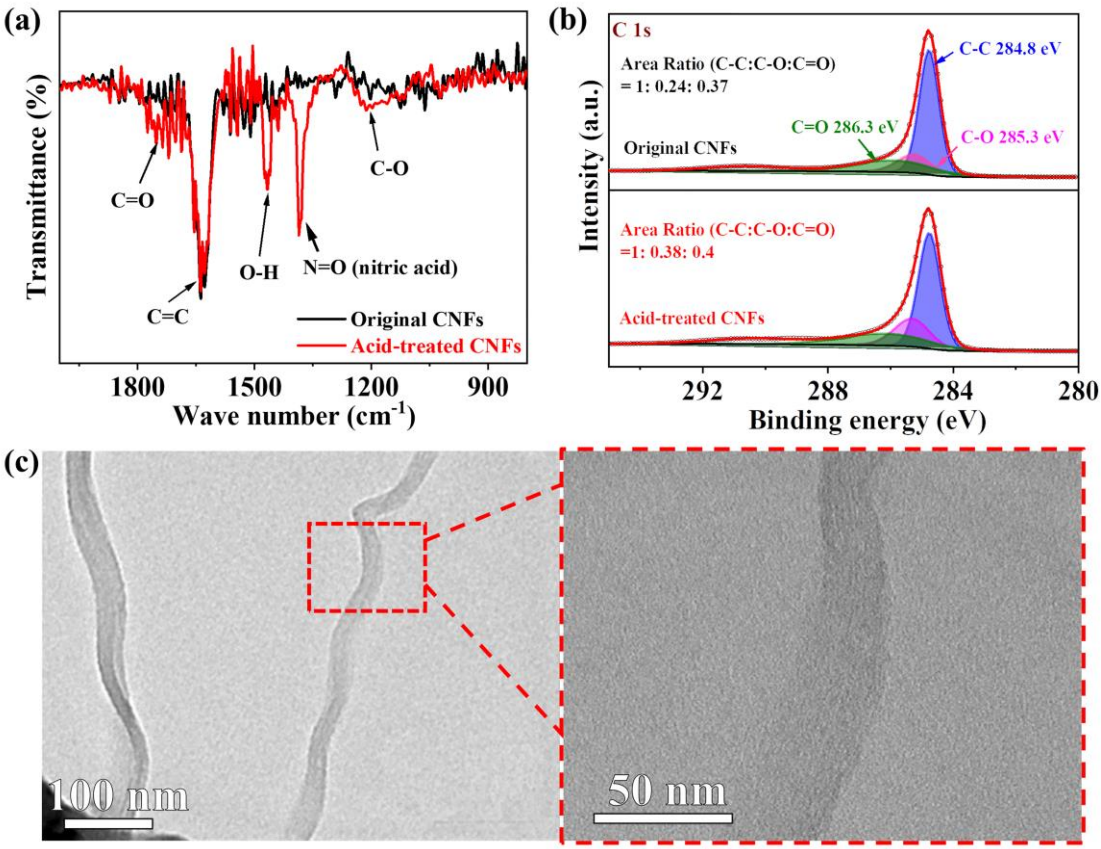

Figure S2. (a) FTIR spectra and (b) high-resolution C 1s XPS spectra of original and acid-treated CNFs. (c) TEM and HRTEM images of acid-treated CNFs.

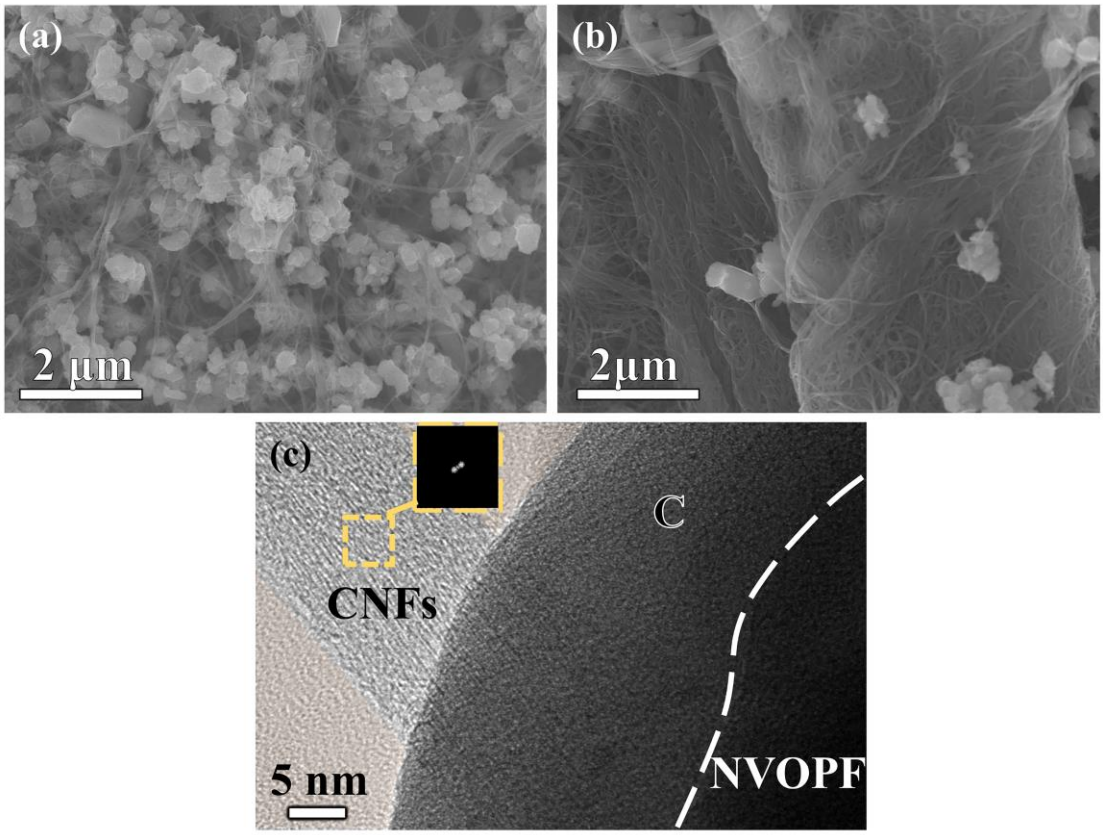

Figure S3. FESEM images of (a) NVOPF@C/CNFs and (b) NVOPF@C&CNFs composite materials by using CNFs with and without acid treatments in advance, respectively. (c) HRTEM image of a primary NVOPF@C/CNFs particle.

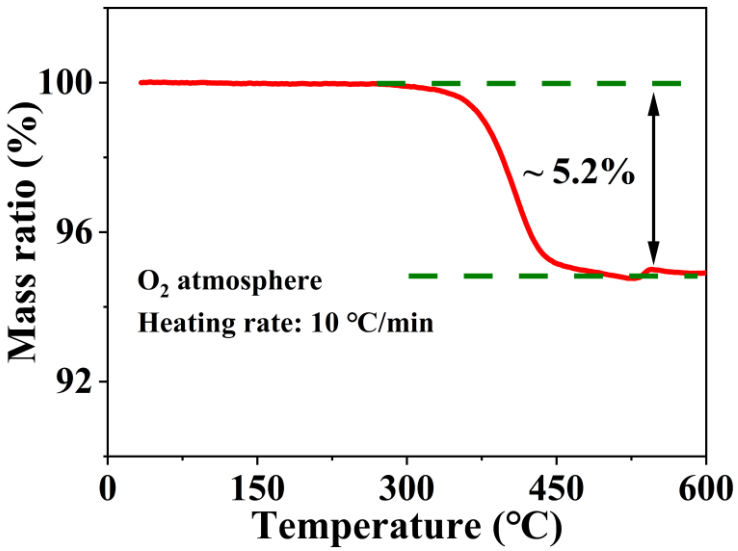

Figure S4. TG curve of the NVOPF@C/CNFs-PA material under a temperature range between room temperature and 600 °C in O_2 flow. The distinct mass loss of 5.2 % between 275 and 525 ℃ can be attributed to the removal of C and CNFs components through burning away in the O_2 flow. The detectable weight increase above 525 ℃ implies the probable decomposition of the NVOPF component without the dual-carbon protection. Hence, the content of C and CNFs components can be quantitatively calculated to be 2.37 and 2.84 %, respectively, within the NVOPF@C/CNFs-PA sample based on the TG analysis and the pre-controlled weight ratio of NVOPF:CNFs being 100:3 for the synthesis.

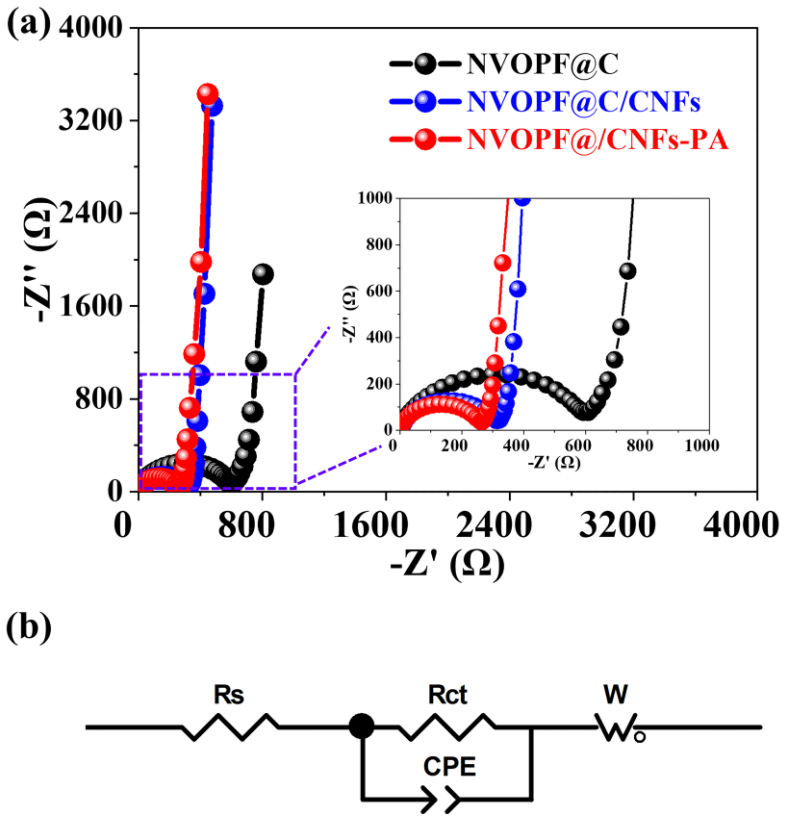

Figure S5. (a) Nyquist plots of three fresh half cells using different NVOPF@C, NVOPF@C/CNFs and NVOPF@C/CNFs-PA cathodes, together with (b) the corresponding equivalent circuit used to simulate different EIS spectra. Where, the R_s stands for the cell resistance in the electrolyte and R_{ct} for the charge transfer resistance. The CPE is a constant phase element, which is related to capacitive behaviors of electrons at an electrode-electrolyte interfaces, and the W is a Warburg impedance, which is associated with Na-ion diffusion within active cathode materials. The R_{ct} values of NVOPF@C, NVOPF@C/CNFs and NVOPF@C/CNFs-PA cathodes were quantitatively extracted to 590.0, 295.3 and 242.9 Ω, respectively.

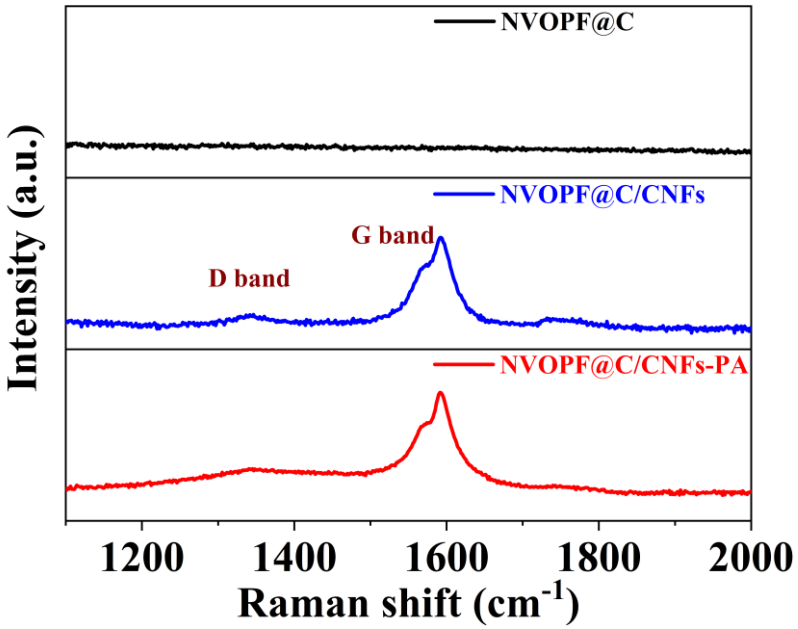

Figure S6. Raman spectra recorded on three different NVOPF@C, NVOPF@C/CNFs and NVOPF@C/CNFs-PA powder samples. The NVOPF@C/CNFs-PA and NVOP@C/CNFs samples show distinct Raman peaks centered at 1345 and 1580 cm^{-1}, corresponding to the D and G bands from the graphitized CNFs component, while the NVOP@C sample has no Raman response, implying the extremely low graphitization degree of the amorphous carbon coating layer.

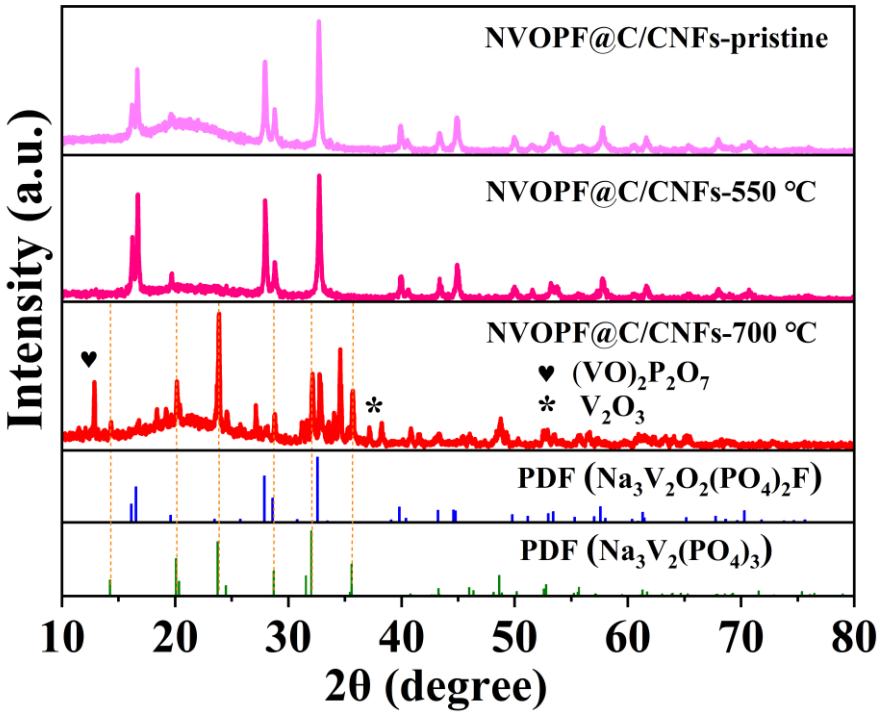

Figure S7. XRD patterns of as-prepared NVOPF@C/CNFs under different heat treatments, indicating its decomposition into $(VO)_2P_2O_7$, $Na_3V_2(PO_4)_3$, V_2O_3 and VF_3 at high post-annealing temperatures.

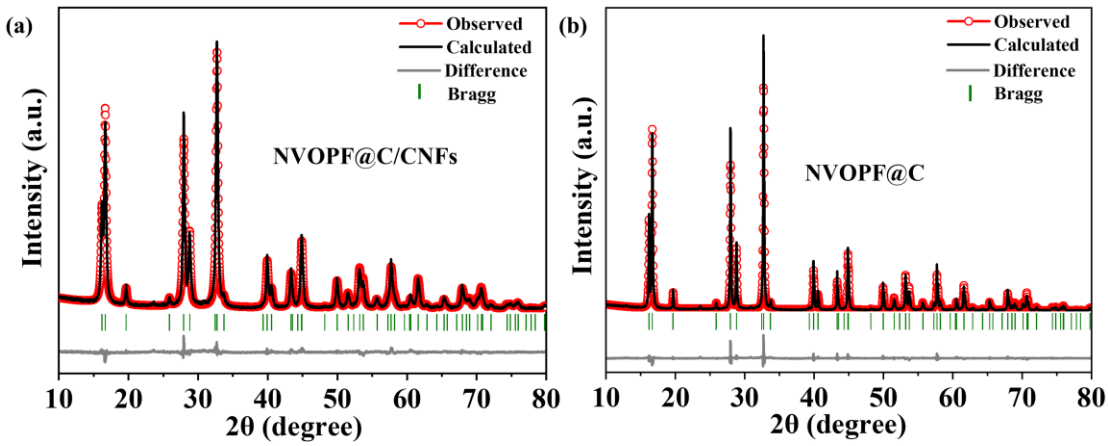

Figure S8. XRD patterns of NVOPF@C and NVOPF@C/CNF materials, in comparison to their calculated patterns by Rietveld refinement. In the plots, red dots are used for the observed data, black lines for calculated data, green bars for Bragg positions, and gray lines for the difference between the observed and calculated data.

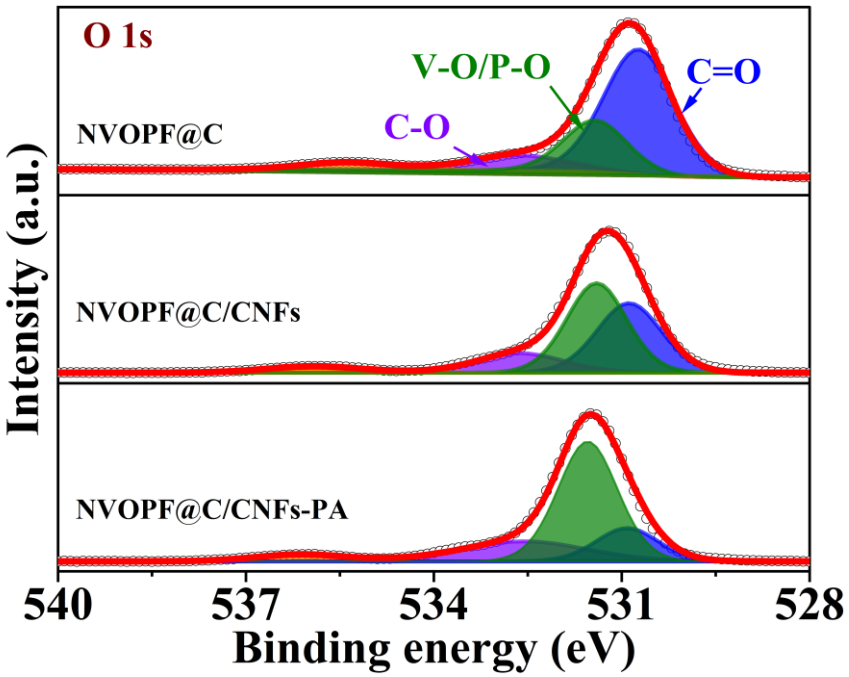

Figure S9. High-resolution O 1s XPS spectra recorded on three different NVOPF@C, NVOPF@C/CNFs and NVOPF@C/CNFs-PA powder samples.

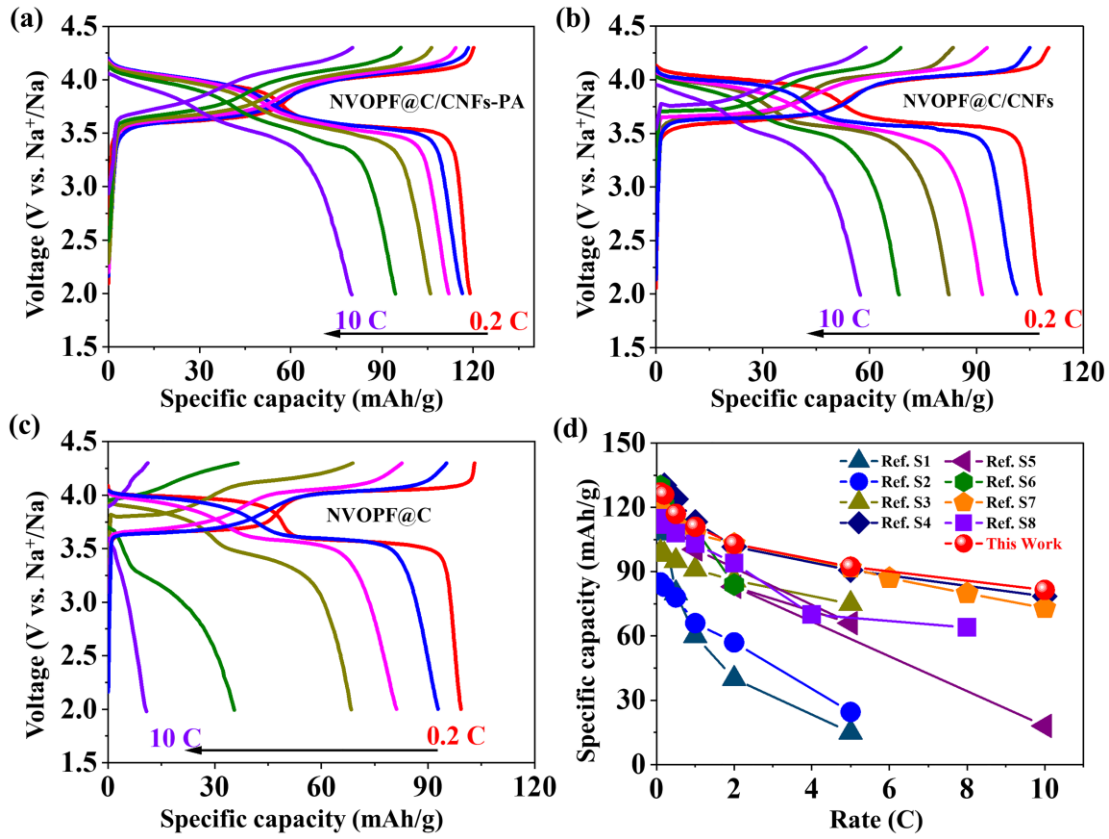

Figure S10. Charge/discharge curves under high C rates up to 10 C of (a) NVOPF@C/CNFs-PA, (b) NVOPF@C/CNFs and (c) NVOPF@C cathodes, and (d) comparative rate performance between this work and reported NVOPF-based cathode materials through different surface engineering in the literature (Table S3).

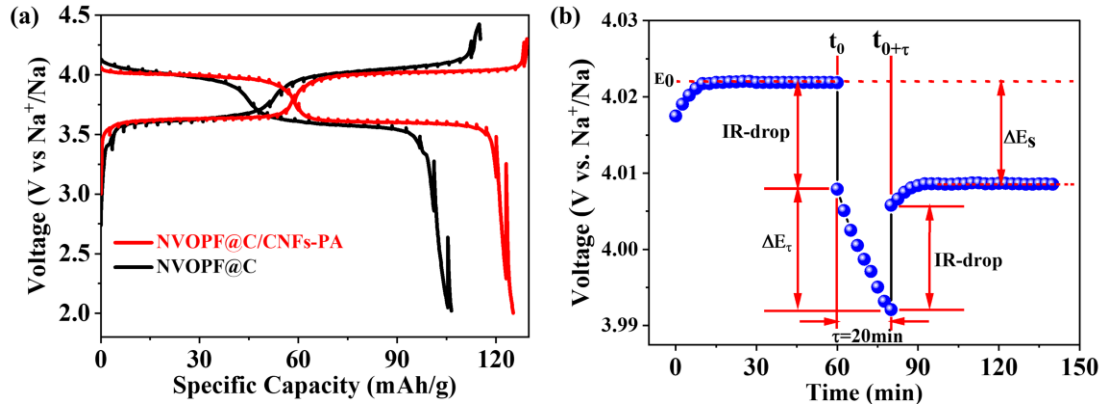

Figure S11. (a) GITT curves of NVOPF@C and NVOPF@C/CNFs-PA cathodes measured under a current pulse of 0.1 C, together with (b) an enlarged voltage profiles for a single step in the GITT curve of the NVOPF@C/CNFs-PA around 4.01 V. The D_{Na^+} can be determined by applying Fick's second law of diffusion based on the GITT analysis and was calculated by the following Eqn.

$$D = \frac{4}{\pi\tau}\left(\frac{m_B V_M}{M_B A}\right)^2 \left(\frac{\triangle E_s}{\triangle E_\tau}\right)^2$$

Where, m_B is the mass loading (g), V_M is the molar volume (cm^3/mol), M_B is the molecular weight (g/mol), A is the contact area of the electrode (cm^2), and τ is the time when the current pulse is applied (s). ΔEs is the voltage difference between the steady-state potentials before and after the current pulse is applied, and ΔEτ refers to the voltage difference between the cell potential at the start and the end of the current pulse as shown in Figure S11b.

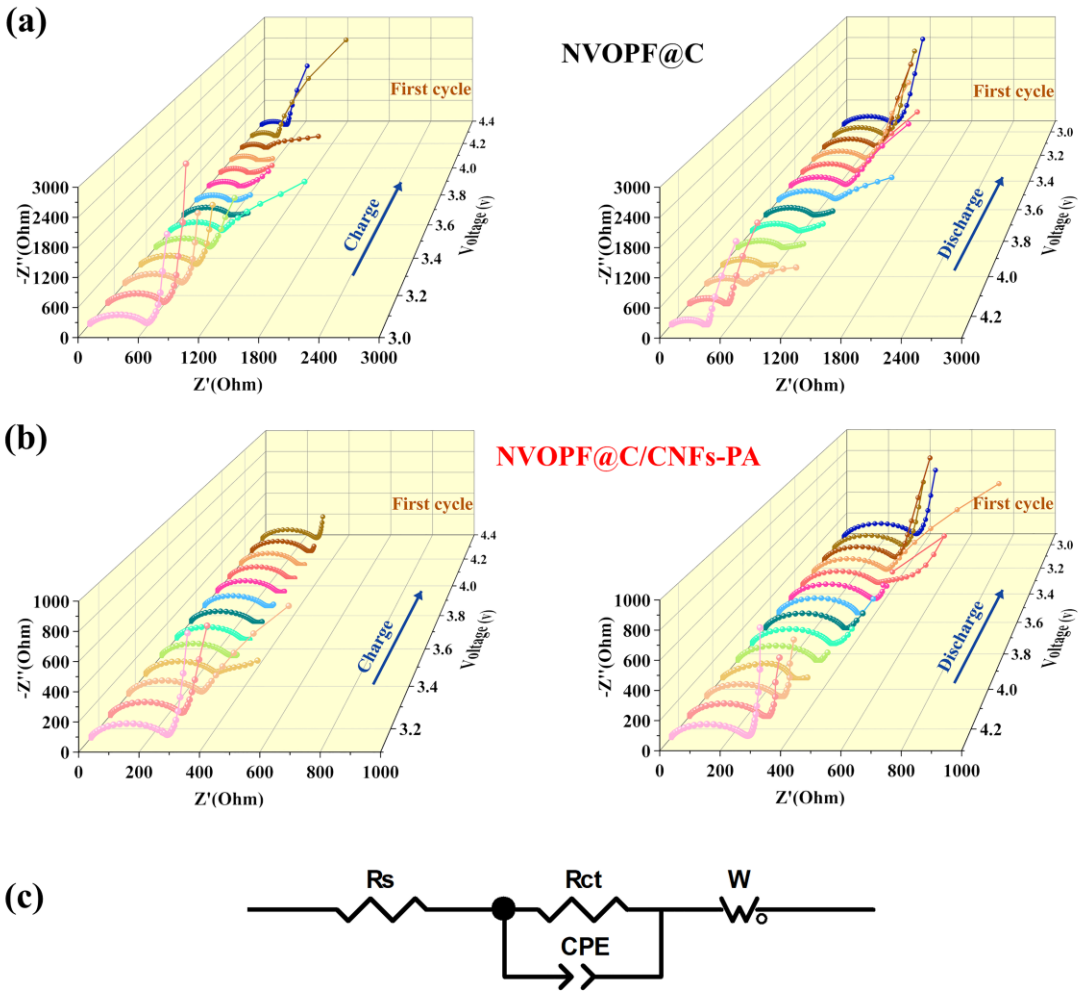

Figure S12. Nyquist plots of (a) NVOPF@C and (b) NVOPF@C/CNFs-PA cathodes as a function of voltages based on *in-situ* EIS measurements in the first cycle, and (c) the corresponding equivalent circuit used to simulate different EIS spectra. Where, the R_s stands for the cell resistance in the electrolyte and R_{ct} for the charge transfer resistance. The CPE is a constant phase element, which is related to capacitive behaviors of electrons at an electrode-electrolyte interfaces, and the W is a Warburg impedance, which is associated with Na-ion diffusion within active cathode materials.

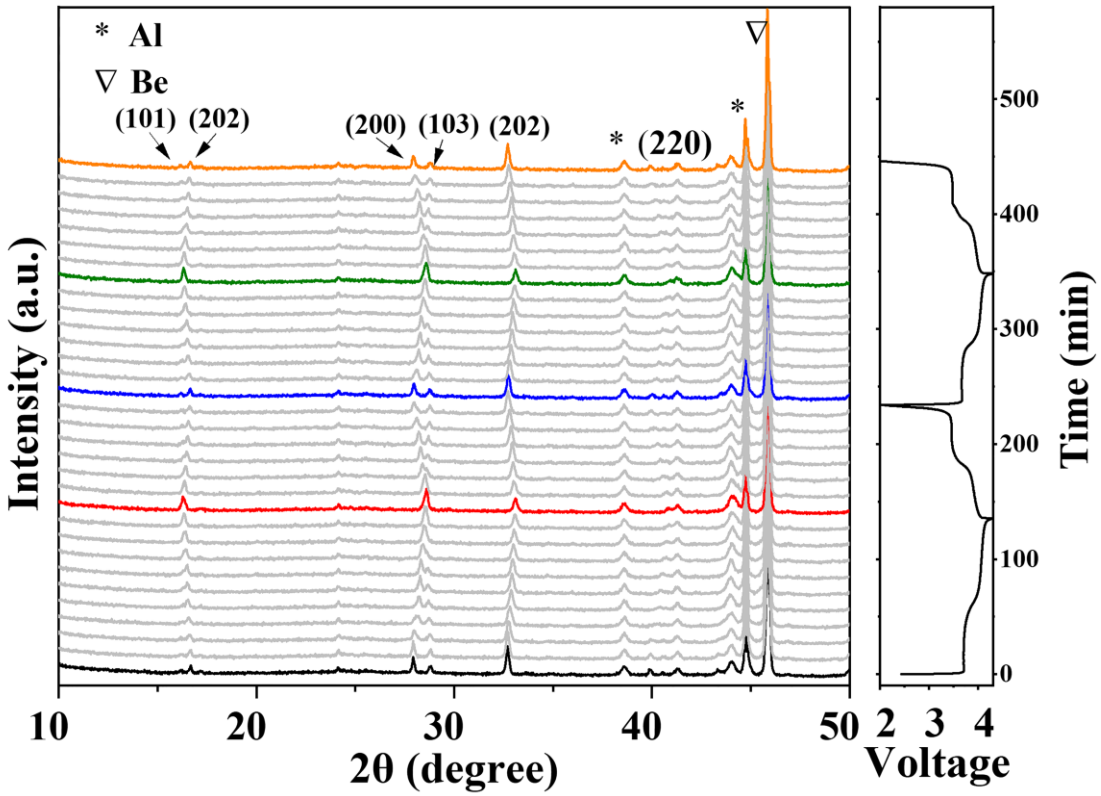

Figure S13. Original XRD patterns recorded during *in-situ* XRD measurements of the NVOPF@C/CNFs-PA cathode for the first two cycles.

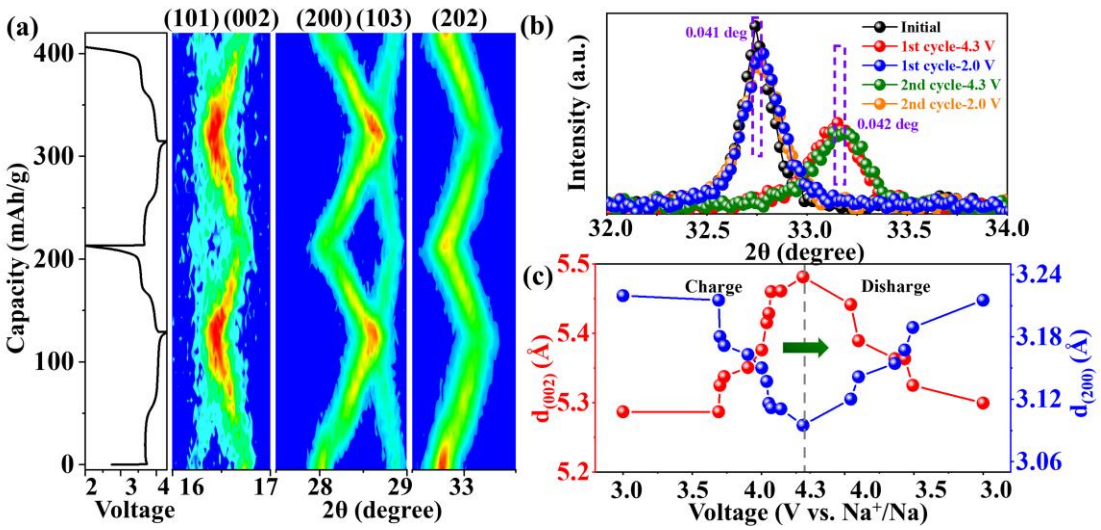

Figure S14. (a) *In-situ* XRD examination during charge/discharge of the NVOPF@C cathode in the first two cycles, showing the recorded charge/discharge curves and contour plots of 101, 002, 200, 103 and 202 reflections, together with (b) corresponding peak shifts of the 202 reflection between fully-discharged 2.0 V and fully-charged 4.3 V during cycling and (c) *d*-spacing changes of (002) and (200) planes based on quantitative refinement analyses on different *in-situ* XRD patterns.

Table S1. Crystallographic parameters for the $Na_3V_2O_2(PO_4)_2F$.

	Wyckoff site	x	y	z	Occ.
Na(1)	8h	0.2548(0)	0.2548(0)	0	0.38
Na(2)	16l	0.3644(7)	0.2369(6)	0	0.19
V	4e	0	0	0.1974(9)	1
P	4d	0.5	0	0.25	1
F	2a	0	0	0	1
O1	16n	0.3105(5)	0	0.1608(0)	1
O2	4e	0	0	0.3556(0)	1

Table S2. Lattice parameters calculated from XRD patterns of NVOPF@C, NVOPF@C/CNFs and NVOPF@C/CNFs-PA samples through quantitative Rietveld refinement analyses.

Samples / Parameters	NVOPF@C	NVOPF@C/CNFs	NVOPF@C/CNFs-PA
a (Å)	6.387(6)	6.378(1)	6.376(3)
b (Å)	6.387 (6)	6.378(1)	6.376(3)
c (Å)	10.637(6)	10.631(1)	10.629(5)
Volume ($Å^3$)	434.04(1)	432.46(8)	432.16(7)
GOF	1.63	1.48	1.41
R_{wp} (%)	8.24	7.22	6.7

Table S3. Comparative rate performance between this work and reported $Na_3V_2O_{2x}(PO_4)_2F_{3-2x}$-based cathode materials through different surface engineering in the literature (RT: room temperature).

Sample	Capacity @C rate	Capacity retention (cycle number@C rate)	Testing temperature	Refs.
NVOPF@C/CNFs-PA	**80.9 mAh/g@10 C**	**81.2% (2500 cycles@5 C)**	**RT**	**This work**
	86.7 mAh/g@50 C	**82.5% (2500 cycles@5 C)**	**60°C**	
NVOPF@TiO_{2-x}	15.3 mAh/g@5 C	___	RT	1
$Na_3(VO)_2(PO_4)_2F$@C	24.5 mAh/g@5 C	___	RT	2
$Na_3V_2O2_x(PO_4)_2F_{3-2x}$/C	75.0 mAh/g@5 C	95.0% (200 cycles@1 C)	RT	3
NVPF@C/G	78.5 mAh/g@10 C	98.9% (40 cycles @1 C)	RT	4
$Na_3V_2O_2(PO_4)_2F$/graphene	66.0 mAh/g@5 C	91.4% (200 cycles@0.1 C)	RT	5
$Na_3V_2(PO_4)_2F_3$	84.0 mAh/g@2 C	88.1% (102 cycles@0.91 C)	RT	6
$Na_3(VOPO_4)_2F$	73.0 mAh/g@10 C	90.0% (1000 cycles@2 C)	RT	7
$Na_3V_2(PO_4)_2F_3$/C	64.0 mAh/g@8 C	___	RT	8
	102.2 mA/g@2 C	93.7% (100 cycles@1 C)	55°C	
$Na_3V_2(PO_4)_2F_3$	64.6 mAh/g@5 C	___	RT	9
	53.85 mA/g@20 C	33.8% (100cycles @2 C)	60°C	
NVPOF	94.9 mAh/g@10 C	___	RT	10
	83.0 mAh/g@30 C	63.44% (200 cycles @0.2 C)	55°C	
$Na_3Fe_{0.3}V_{1.7}O(PO_4)_2F_2$	118.0 mAh/g@1 C	___	RT	11
	110 mAh/g@1 C	10.0% (60 cycles@0.2 C)	45°C	
NVPF	102.1 mA/g@2 C	72.0% (60 cycles@0.1 C)	55°C	12
NVOPF@PEDOT	50.0 mAh/g@20 C	83.8% (8000cycles@5 C)	RT	13
CNF@NVPF	64.9 mAh/g@20 C	96.0% (2000 cycles@10 C)	RT	14
$Na_3V_2O_2(PO_4)_2F$-MWCNT	60.0 mAh/g@20 C	89.1% (120 cycles @0.1 C)	RT	15
NVPF@rGO	53.0 mAh/g@30 C	98.0% (2000 cycles @20 C)	RT	16
CNF@NVPF	56.0 mAh/g@20 C	87.0% (500 cycles@5 C)	RT	17

References

1. P. Du, T. Li, X. Jiang, D. Wang and X. Zheng, *J. Alloys Compd.*, 2020, **814**, 152270.
2. P. Serras, V. Palomares, P. Kubiak, L. Lezama and T. Rojo, *Electrochem. Commun.*, 2013, **34**, 344-347.
3. P. Serras, V. Palomares, A. Goñi, P. Kubiak and T. Rojo, *J. Power Sources*, 2013, **241**, 56-60.
4. H. Jin, J. Dong, E. Uchaker, Q. Zhang, X. Zhou, S. Hou, J. Li and G. Cao, *J. Mater. Chem. A*, 2015, **3**, 17563-17568.
5. M. Xu, L. Wang, X. Zhao, J. Song, H. Xie, Y. Lu and J. B. Goodenough, *Phys. Chem. Chem. Phys.*, 2013, **15**, 13032-13037.
6. W. Song, X. Ji, Z. Wu, Y. Zhu, F. Li, Y. Yao and C. E. Banks, *RSC Adv.*, 2014, **4**, 11375-11383.
7. Y. Qi, L. Mu, J. Zhao, Y. S. Hu, H. Liu and S. Dai, *Angew. Chem. Int. Ed.* , 2015, **54**, 9911-9916.
8. L. Deng, G. Sun, K. Goh, L.-L. Zheng, F.-D. Yu, X.-L. Sui, L. Zhao and Z.-B. Wang, *Electrochim. Acta*, 2019, **298**, 459-467.
9. J. Hwang, K. Matsumoto and R. Hagiwara, *Advanced Energy Materials*, 2020, **10**, 2001880.
10. X. X. Zhao, Z. Y. Gu, W. H. Li, X. Yang, J. Z. Guo and X. L. Wu, *Chemistry*, 2020, **26**, 7823-7830.
11. R. Essehli, K. Maher, R. Amin, A. Abouimrane, A. Mahmoud, N. Muralidharan, R. K. Petla, H. B. Yahia and I. Belharouak, *ACS Appl. Mater. Interfaces*, 2020, **12**, 41765-41775.
12. G. Yan, K. Reeves, D. Foix, Z. Li, C. Cometto, S. Mariyappan, M. Salanne and J. M. Tarascon, *Adv. Energy Mater.*, 2019, **9**, 1901431.
13. L. Wu, S. Dong, G. Pang, H. Li, C. Xu, Y. Zhang, H. Dou and X. Zhang, *J. Mater. Chem. A*, 2019, **7**, 1030-1037.
14. R. Qiu, R. Fei, J.-Z. Guo, R. Wang, B. He, Y. Gong, X.-L. Wu and H. Wang, *J. Power Sources*, 2020, **466**, 228249.
15. P. R. Kumar, Y. H. Jung, J. E. Wang and D. K. Kim, *J. Power Sources*, 2016, **324**, 421-427.
16. Y. Cai, X. Cao, Z. Luo, G. Fang, F. Liu, J. Zhou, A. Pan and S. Liang, *Adv. Sci.*, 2018, **5**, 1800680.
17. Z. Mao, R. Wang, B. He, Y. Gong and H. Wang, *Small*, 2019, **15**, 1902466.